

Anti-chiral edge states in Heisenberg ferromagnet on a honeycomb lattice

Dhiman Bhowmick and Pinaki Sengupta
*School of Physical and Mathematical Sciences,
 Nanyang Technological University, Singapore*

(Dated: October 8, 2022)

We demonstrate the emergence of anti-chiral edge states in a Heisenberg ferromagnet with Dzyaloshinskii-Moriya interaction (DMI) on a honeycomb lattice with inequivalent sublattices. The DMI, which acts between atoms of the same species, differs in magnitude for the two sublattices, resulting in a shifting of the energy of the magnon bands in opposite directions at the two Dirac points. The chiral symmetry is broken and for sufficiently strong asymmetry, the band shifting leads to anti-chiral edge states (in addition to the normal chiral edge states) in a rectangular strip where the magnon current propagates in the same direction along the two edges. This is compensated by a counter-propagating bulk current that is enabled by the broken chiral symmetry. We analyze the resulting magnon current profile across the width of the system in details and suggest realistic experimental probes to detect them. Finally, we propose a material that can potentially exhibit such anti-chiral edge states.

PACS numbers: 85.75.-d, 75.47.-m, 73.43.-f, 72.20.-i

Introduction.- Quantum magnets have emerged as a versatile platform for realizing magnetic analogs of the plethora of topological phases that have been predicted, analyzed, classified and observed in electronic systems over the past decade. Haldane's paradigmatic model¹ of tight binding electrons on a honeycomb lattice with complex next-nearest neighbor hopping – that constitutes the foundation of many of the electronic topological phases – has a natural realization in (quasi-) 2D insulating ferromagnets such as CrI_3 ² and $\text{AFe}_2(\text{PO}_4)_2$ ($\text{A}=\text{Ba}, \text{Cs}, \text{K}, \text{La}$)³. In many of these materials, the dominant Heisenberg exchange is supplemented by a next-nearest neighbor anti-symmetric Dzyaloshinskii-Moriya interaction (DMI). Magnetic excitations in these systems are described by two species of quasiparticles – spinons with up and down spins. The Kane-Mele-Haldane model – analogous to the Kane Mele model for electrons – has been proposed to describe the spinons over a wide range of temperatures.⁴ The spinon bands acquire a non-trivial dispersion due to Berry phase arising from the DMI. This results in a spin Nernst effect (SNE) where a thermal gradient drives a transverse spin current, a spinon version of the spin Hall effect⁴⁻⁷. In a finite sample, the two spinon species generate two counterpropagating spin currents along the edges that are protected by chiral symmetry of the Hamiltonian – analogous to two copies of the thermal Hall effect (THE) of magnons that has been observed in many insulating magnets⁸⁻¹¹.

Recently, there has been growing interest in engineering systems with co-propagating edge currents¹²⁻¹⁴, through an ingenious, yet physically unrealistic, modification of the Haldane model. The conservation of net current is satisfied by counter propagating bulk current. That is, the bulk is not insulating, in contrast to conventional topological insulators. In this work, we demonstrate that anti-chiral states arise naturally in spinons on a honeycomb magnet comprised of two different mag-

netic ions, with unequal DMI for the two sublattices. In the absence of DMI, the spinon dispersion consists of two doubly degenerate bands with linear band crossings at \mathbf{K} and \mathbf{K}' ¹⁵. A finite DMI lifts the degeneracy between the two spinon branches and opens up a gap in the spectrum¹⁶⁻¹⁹. For *asymmetric* DMI, the two bands for each spinon species are shifted in opposite directions relative to each other at the \mathbf{K} and \mathbf{K}' points in the Brillouin zone. This results in similar dispersion for the gapless modes at both edges, giving rise to co-propagating edge states. This is shown to yield effective anti-chiral edge states for the spinons in addition to normal chiral ones. We present a detailed characterization of the nature of the edge and bulk spinon states and suggest suitable experimental signatures to detect these novel topological states.

Model.- We consider a Heisenberg ferromagnet on the honeycomb lattice with unequal DMI (D_A and D_B) on the two sub-lattices. Introducing the symmetric and anti-symmetric combinations of D_A and D_B as, $D = \frac{1}{2}(D_A + D_B)$, $D' = \frac{1}{2}(D_A - D_B)$ – termed chiral and anti-chiral DMI respectively for reasons that will become clear later – the Hamiltonian is given by,

$$\mathcal{H} = -J \sum_{\langle i,j \rangle} \mathbf{S}_i \cdot \mathbf{S}_j + D \sum_{\langle\langle i,j \rangle\rangle} \nu_{ij} \hat{z} \cdot (\mathbf{S}_i \times \mathbf{S}_j) + D' \sum_{\langle\langle i,j \rangle\rangle} \nu'_{ij} \hat{z} \cdot (\mathbf{S}_i \times \mathbf{S}_j) - B \sum_i S_i^z, \quad (1)$$

where, $J > 0$ is the nearest neighbor Heisenberg interaction and $\nu_{ij} = +1$ when i and j are along the cyclic arrows shown in Fig.1(b). Finally, $\nu'_{ij} = +\nu_{ij}$ for sublattice-A and $\nu'_{ij} = -\nu_{ij}$ for sublattice-B. The magnetic field B is introduced in a Zeeman coupling term to stabilize the ferromagnetic ground state at finite temperature.

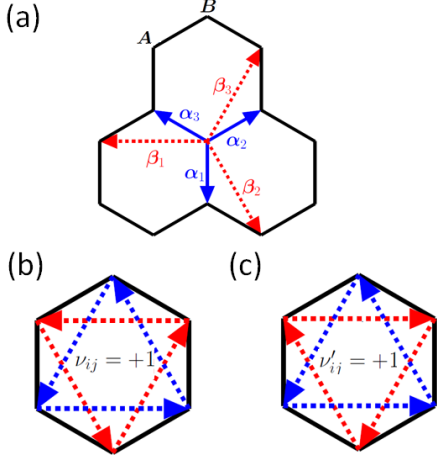


FIG. 1: (color online)(a) The honeycomb lattice structure. (b) The directions along which $\nu_{ij} = +1$ has been shown, otherwise $\nu_{ij} = -1$. (c) The directions along which $\nu'_{ij} = +1$ has been shown, otherwise $\nu'_{ij} = -1$.

The ground state of the hamiltonian (Eq.1) is ferromagnetic for $J > -\frac{3\sqrt{3}}{2} \sum_s |D + sD'|$, $s = \pm 1$. We apply the Schwinger Boson mean field theory (SBMFT) to study the topological character of the low energy magnetic excitations at a finite temperature. The Schwinger Boson representation consists of the mapping the spin operators into spinons as, $S_i^+ = c_{i,\uparrow}^\dagger c_{i,\downarrow}$, $S_i^- = c_{i,\downarrow}^\dagger c_{i,\uparrow}$, $S_i^z = \frac{1}{2} (c_{i,\uparrow}^\dagger c_{i,\uparrow} - c_{i,\downarrow}^\dagger c_{i,\downarrow})$, where $c_{i,s}$ and $c_{i,s}^\dagger$ are the annihilation and creation operators of spin-1/2 up or down spinons respectively. The constraint $\sum_s c_{i,s}^\dagger c_{i,s} = 2S$, $\forall i$ on the bosonic operators ensures the fulfillment of the spin-S algebra.

After applying Schwinger Boson transformation along with the constraint, and using a mean field approximation to reduce the 4-body operators to bilinear forms, the spin model Eq.1 is mapped to the the mean field hamiltonian,

$$\begin{aligned} \mathcal{H} = & -\eta J \sum_{\langle i,j \rangle, s} [\hat{c}_{i,s}^\dagger \hat{c}_{j,s} + \text{H.c.}] + \sum_{i,s} \left(\lambda - \frac{sB}{2} \right) \hat{c}_{i,s}^\dagger \hat{c}_{i,s} \\ & + \frac{D}{2} \sum_{\langle\langle ij \rangle\rangle, s} [(i\nu_{ij}s\zeta_{-s} + s\xi_{-s}) \hat{c}_{i,s}^\dagger \hat{c}_{j,s} + \text{H.c.}] \\ & + \frac{D'}{2} \sum_{\langle\langle ij \rangle\rangle, s} [(i\nu'_{ij}s\zeta_{-s} + s\xi'_{-s}) \hat{c}_{i,s}^\dagger \hat{c}_{j,s} + \text{H.c.}] \quad (2) \end{aligned}$$

where the mean field parameters are defined as, $\eta = \sum_s \langle \hat{\chi}_{ij,s} \rangle \equiv \sum_s \langle \hat{c}_{i,s}^\dagger \hat{c}_{j,s} \rangle$ evaluated on the nearest neighbour-bonds, and $\zeta = \zeta' = \frac{1}{2} \langle \hat{\chi}_{ij,s} + \hat{\chi}_{ji,s} \rangle$, $\xi = \frac{\nu_{ij}}{2i} \langle \hat{\chi}_{ij,s} - \hat{\chi}_{ji,s} \rangle$ and $\xi' = \frac{\nu'_{ij}}{2i} \langle \hat{\chi}_{ij,s} - \hat{\chi}_{ji,s} \rangle$, evaluated on next nearest neighbour bonds. The terms associated with the parameters $\eta, \nu_{ij}\zeta_{-s}$ of spinon Hamiltonian Eq2

constitute the Kane-Mele-Haldane model⁴. The term with parameter $\nu'_{ij}\zeta_{-s}$ corresponds to the anti-chiral hopping term introduced in Ref.12. The terms with the parameters ξ_s and ξ'_s have no effect on the energy or the topological character of the bands, as the parameters are found to be much smaller compared to other mean field parameters. λ is the Lagrange undetermined multiplier introduced to implement the local constraint. The physical significance of the mean field parameters and the SBMFT method is described in supplementary material.

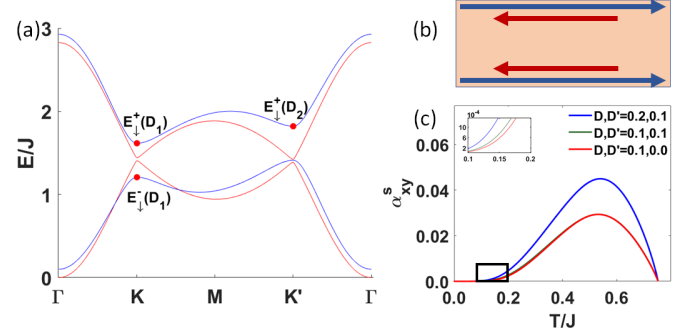


FIG. 2: (color online)(a) band along symmetry lines $\Gamma K, KM, MK', K'\Gamma$ for $J = 1.0, B = 0.1, D_{ch} = 0.1, D_{Ach} = 0.05, T = 0.25$. The blue band is for down-spinon band and the red band is for up-spinon band. (b) The schematic of the antichiral contribution of the current from edge-states (blue arrows) and bulk-states (red arrows). (c) Nernst-conductivity v.s. temperature plot for different DM-interactions. The inset shows magnified figure of the rectangular portion of the figure.

Results.- Band structure for spinons at a temperature $T=0.25J$ is shown in Fig.2(a). In the absence of DMI, the two bands cross linearly at the Dirac points \mathbf{K} and \mathbf{K}' ¹⁵ – a finite DMI opens up a gap with magnitude $\Delta_s = 3\sqrt{3}|D\zeta_{-s}|$ in each spinon sector at \mathbf{K} and \mathbf{K}' .^{4,16–19} For *anisotropic* system ($D_A \neq D_B$) considered here, the gap opening is not symmetric and leads to a *tilting* of the spinon bands near the Dirac momenta. The band tilting for each band in each spinon sector, defined as the energy difference between two Dirac-points in the same band, is given by, $T_s^r = 3\sqrt{3}|D'\zeta_{-s}|$. While the anti-chiral DM-interaction drives the tilting of the bands, it has no effect on the magnitude of the band gap. Crucially, the tilting is opposite for the two species of spinons. For the parameters chosen in Fig.2(a), the gap and tilting for the up-spinon bands are smaller compared to those for the down spinon bands. This is because in the presence of positive magnetic field $B = 0.1$ considered here, there are fewer down spinons and consequently, $\zeta_{\downarrow} < \zeta_{\uparrow}$.

The bands in each spinon sectors carry non-zero Berry curvature. Spin Nernst effect has been proposed as a physical phenomenon to identify Berry curvature of spinon bands when there are comparable numbers of up and down spinons. Here we explore whether it can detect the existence of anti-chiral DM-interaction. The Nernst

conductivity has been calculated using the expression $\alpha_{xy}^s = \frac{1}{2V} \sum_{\mathbf{k}, s, \tau} s c_1 [\rho_s^T(\mathbf{k})] \Omega_s^T(\mathbf{k})$ ^{4,20}. The results are plotted in Fig.2(c) for different D and D' . Increase in D increases the band gap as well as the Berry curvature away from the Dirac-points. As a result, the Nernst conductivity is substantially effected by the D (Fig.2(c)). Conversely, since the Berry curvature is independent of the anti-chiral DM-term, D' , it has very little effect in the Nernst conductivity. So, the presence of antichiral DM-term in the system is very hard to detect using Nernst conductivity. Instead, we suggest an alternative way to detect the presence of antichiral DM-term.

The gapped bands are topologically non-trivial with Chern numbers $C_{\uparrow}^{-} = +1, C_{\uparrow}^{+} = -1, C_{\downarrow}^{-} = -1, C_{\downarrow}^{+} = +1$ ²¹. Due to bulk-edge correspondence, we expect to observe edge states in a finite system. In the isotropic limit ($D_A = D_B$), the edge states are topologically protected by a chiral symmetry. The spinon currents along the two edges are equal and opposite for the up and down spinons. This results in a net flow of spins along the two edges in opposite directions – any scattering to the bulk states is prevented by symmetry constraints. For the asymmetric system considered here, D' induces an anti-chiral edge current of spinons where each species of spinon flows in the same direction along the two edges. This is balanced by counterflow current of spinons in the opposite direction carried by the bulk modes. The anti-chiral DMI breaks the chiral symmetry protecting the edge states and enables scattering between edge and bulk states. This edge-to-bulk scattering produces the bulk current that balances the anti-chiral edge current. In the following we discuss how the bulk and edge state dispersion changes due to interplay between the chiral and anti-chiral DM-interaction.

Fig. 3 shows the spinon bands for a honeycomb nano-ribbon with dimension 200×500 lattice sites with zigzag edges, together with the spin current profile along the width of the ribbon. Three different sets of (D, D') are chosen to illustrate the evolution of band dispersion and spin currents with changing DMI. For clarity of presentation, only one species of spinons are illustrated. Along with the total spin current, the contributions from the bulk and two edge modes are calculated separately to identify the effects of D' on each component. Finally, the spinon bands and the individual spin currents are color coded for easy identification. Green is used to represent the bulk bands and their contribution to the spin current at each position along the width of the ribbon; red (blue) denotes the localized spinon mode and the associated spin current at the top (bottom) edge. A negative (positive) value of the spin current denote spinon transport to the left (right) along the length of the ribbon.

For $D > D'$, the tilting of the bands is small and the dispersion of edge states at upper and lower edges are opposite, as shown in the Fig.3(c). The edge states are predominantly chiral in nature, and the spin current at the two edges are opposite in direction (though not equal in magnitude due to $D' \neq 0$, which breaks chiral symme-

try). Because of $U(1)$ -symmetry of each spinon sector, there is a counter-propagating bulk current to compensate the imbalance between edge states. However, the bulk current is not uniform across the width of the ribbon. Instead, it is primarily confined to a small region near the edges. At each edge, the bulk current opposes the edge current, with its magnitude decreasing rapidly away from the edges.

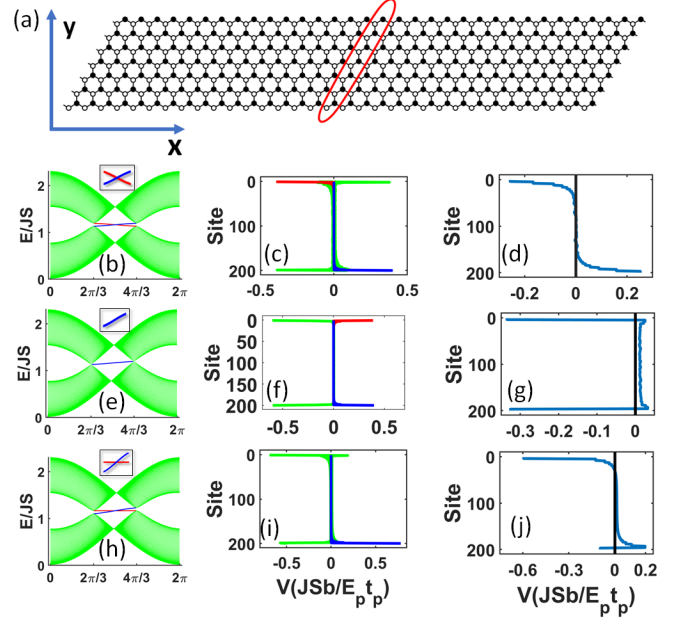


FIG. 3: (color online)(a) A honeycomb ribbon. The encircled sites are the basis of unit cell. The figure sets $\{(b) - (d)\}, \{(e) - (g)\}, \{(h) - (j)\}$ represents result for down-spinon from 200×500 stripe with DM-interactions $\{D = 0.1, D' = 0.001\}, \{D = 0.001, D' = 0.1\}, \{D = 0.1, D' = 0.1\}$ respectively. The other parameters are $J = 1.0, B = 0.1, T = 0.5$ for all the plots. The figure sets $\{(b), (e), (h)\}$ shows the band structure and inset of the figures shows the magnified dispersion of the edge states. The figure sets $\{(e), (f), (g)\}$ gives the spatial current distribution along width of the stripe. The figure sets $\{(d), (g), (j)\}$ shows the average of spatial current distribution over four sites respectively. In the figure sets $\{(b), (c), (e), (f), (h), (i)\}$ the green, red and blue plots corresponds to bulk-state, upper edge edge-state and lower-edge edge-state respectively. Moreover, the results for up-spinon is qualitatively same, the only difference is the dispersions are opposite for the bulk and edge states.

For large anti-chiral component of the DMI ($D' \gg D$), the tilting of the bands at the Dirac points is much greater and yields identical dispersion for the two edge states (Fig. 3(e)). This results in *anti*-chiral edge states where the spin current is in the same direction along both edges of the ribbon (Fig. 3(f)). This is balanced by a counter-propagating bulk current.

Once again, the bulk current is primarily confined to the edges (Fig. 3(f)). The total current distribution along the cross section of the ribbon is highly asymmetric, with a large spin current along the two edges along the same direction and a small, but finite current in the bulk in the opposite direction.

Finally, when the chiral and anti-chiral components of the DMI are comparable in magnitude ($D \approx D'$), one of the edge states (the top edge in the present case) acquires a dispersionless character (Fig. 3(h)). In other words, the edge state at the top is localized with no spinon transport while the bottom edge has a finite dispersion with a finite edge current (Fig. 3(i)). The bulk states provide the necessary counter-current to maintain S_z conservation. The resulting spin current profile is once again highly asymmetric and varies greatly across the cross section of the ribbon, as illustrated in (Fig. 3(j)). However, the current profile is distinct from that observed for $D' \gg D$. Hence, a detailed analysis of the current profile across the nano-ribbon may be used to identify the presence of a significant anti-chiral DMI.

We suggest that magnetic force microscopy (MFM) offers a promising experimental technique to measure the spinon current across the nano-ribbon and hence detect the presence of anti-chiral edge states. Current MFM techniques can probe the local spin current in a finite sample to a resolution of a few nm. Since the topological character of the spinon bands for the different ranges of anisotropic DMI is reflected in distinct current profile across the ribbon, we believe MFM provides a promising experimental technique to identify anti-chiral edge states in real quasi-2D materials.

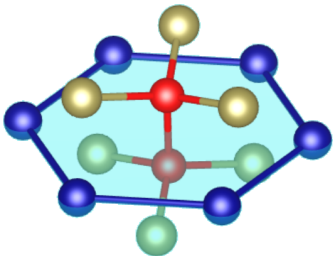


FIG. 4: (color online) A section of ferromagnetic honeycomb plan of CrSiTe_3 , where Cr is in blue, Si is in red, Te is in yellow.

Material Realizaion.— Recently, several Cr-based weakly Van Der Waals coupled honeycomb ferromagnets with DM-interaction have been realized. Of these, CrI_3 ² and CrBr_3 ^{22–24} have a space group symmetry $R\bar{3}$, and the Cr-ions are all equivalent. However, anti-chiral edge states require two in-equivalent sub-lattices (with $D_A \neq D_B$). The materials CrSrTe_3 ²⁵ and CrGeTe_3 ²⁶ have a space group $R3$, with putatively two distinct Cr ions, but that dissimilarity arises from two in-equivalent ferromagnetic layers. The inter-layer coupling is due to VdW force and so we do not expect strong inter-layer spin-interaction. Hence none of these materials in their native states are suitable for realizing anti-chiral edge states. We propose a way to break the equivalence between Cr-ions of two sub-lattices, starting with CrSiTe_3 . The material consists of 2D layers of Cr ions arranged on a honeycomb lattice with two apical Si ions and three Te ions connected to each Si ion located symmetrically on each side of the honeycomb plane (Fig. 4). The crystal possesses an S_6 symmetry – each Cr-ion can be mapped to another Cr-ion by a six-fold rotation about an axis perpendicular to the honeycomb plane and passing through the Si atoms, followed by a mirror reflection with respect to the honeycomb plane. Our idea is to replace one Si with a Ge-atom. Such a substitution will break the S_6 symmetry, although a C_3 symmetry is retained. This is expected to result in $D_A \neq D_B$ that is required for the emergence of anti-chiral edge states. To summarize, we propose a crystal like $\text{CrGe}_x\text{Si}_{1-x}\text{Te}_3$, which will have a ferromagnetic honeycomb structure with in-equivalent sub-lattices and represents our model. Based on similar symmetry arguments the materials $\text{AFe}_2(\text{P}_x\text{D}_{1-x}\text{O}_4)_2$ ($A=\text{Ba, Cs, K, La}$ and $D=\text{N, As, Sb}$) are also a promising candidates for realizing anti-chiral edge states.

In conclusion, we have studied a Heisenberg ferromagnet with additional next nearest neighbor DM interactions on a honeycomb lattice with broken sublattice symmetry. The unequal DM interaction between atoms on different sublattices, together with the broken chiral symmetry results in the emergence of anti-chiral edge states, in addition to the normal chiral modes. This is manifested in unique spin current distribution across the width of a finite system with ribbon geometry. We propose experimental probes to detect the presence of anti-chiral edge states as well as a potential material where such states may be realized experimentally.

Financial support from the Ministry of Education, Singapore, in the form of grant MOE2016-T2-1-065 is gratefully acknowledged.

¹ F. D. M. Haldane, *Phys. Rev. Lett.* **61**, 1029 (1988).

² L. Chen, J.-H. Chung, B. Gao, T. Chen, M. B. Stone, A. I. Kolesnikov, Q. Huang, and P. Dai, *Phys. Rev. X* **8**, 041028 (2018).

³ H.-S. Kim and H.-Y. Kee, *npj Quantum Materials* **2**, 20 (2017).

⁴ S. K. Kim, H. Ochoa, R. Zarzuela, and Y. Tserkovnyak, *Phys. Rev. Lett.* **117**, 227201 (2016).

⁵ V. A. Zyuzin and A. A. Kovalev, *Phys. Rev. Lett.* **117**, 217203 (2016).

⁶ R. Cheng, S. Okamoto, and D. Xiao, *Phys. Rev. Lett.* **117**, 217202 (2016).

- ⁷ Y. Zhang, S. Okamoto, and D. Xiao, *Phys. Rev. B* **98**, 035424 (2018).
- ⁸ Y. Onose, T. Ideue, H. Katsura, Y. Shiomi, N. Nagaosa, and Y. Tokura, *Science* **329**, 297 (2010).
- ⁹ M. Hirschberger, J. W. Krizan, R. J. Cava, and N. P. Ong, *Science* **348**, 106 (2015).
- ¹⁰ T. Ideue, Y. Onose, H. Katsura, Y. Shiomi, S. Ishiwata, N. Nagaosa, and Y. Tokura, *Phys. Rev. B* **85**, 134411 (2012).
- ¹¹ R. Hentrich, M. Roslova, A. Isaeva, T. Doert, W. Brenig, B. Büchner, and C. Hess, *Phys. Rev. B* **99**, 085136 (2019).
- ¹² E. Colomés and M. Franz, *Phys. Rev. Lett.* **120**, 086603 (2018).
- ¹³ S. Mandal, R. Ge, and T. C. H. Liew, *Phys. Rev. B* **99**, 115423 (2019).
- ¹⁴ M. Vila, N. T. Hung, S. Roche, and R. Saito, *Phys. Rev. B* **99**, 161404(R) (2019).
- ¹⁵ S. S. Pershoguba, S. Banerjee, J. C. Lashley, J. Park, H. Ågren, G. Aeppli, and A. V. Balatsky, *Phys. Rev. X* **8**, 011010 (2018).
- ¹⁶ S. A. Owerre, *Journal of Physics Condensed Matter* **28**, 386001 (2016).
- ¹⁷ S. A. Owerre, *Journal of Applied Physics* **120**, 043903 (2016).
- ¹⁸ S. A. Owerre, *Journal of Physics Communications* **1**, 021002 (2017).
- ¹⁹ P. A. Pantaleón, R. Carrillo-Bastos, and Y. Xian, *Journal of Physics: Condensed Matter* **31**, 085802 (2019).
- ²⁰ A. A. Kovalev and V. Zyuzin, *Phys. Rev. B* **93**, 161106(R) (2016).
- ²¹ E. Matsuoka, K. Hayashi, A. Ikeda, K. Tanaka, T. Takabatake, and M. Matsumura, *Journal of the Physical Society of Japan* **74**, 1382 (2005).
- ²² E. J. Samuelsen, R. Silbergliitt, G. Shirane, and J. P. Remika, *Phys. Rev. B* **3**, 157 (1971).
- ²³ I. Tsubokawa, *Journal of the Physical Society of Japan* **15**, 1664 (1960).
- ²⁴ T. J. Williams, A. A. Aczel, M. D. Lumsden, S. E. Nagler, M. B. Stone, J.-Q. Yan, and D. Mandrus, *Phys. Rev. B* **92**, 144404 (2015).
- ²⁵ T. J. Williams, A. A. Aczel, M. D. Lumsden, S. E. Nagler, M. B. Stone, J.-Q. Yan, and D. Mandrus, *Phys. Rev. B* **92**, 144404 (2015).
- ²⁶ C. Gong, L. Li, Z. Li, H. Ji, A. Stern, Y. Xia, T. Cao, W. Bao, C. Wang, Y. Wang, Z. Qiu, R. Cava, S. G. Louie, J. Xia, and X. Zhang, *JTh5C.2* (2017).